Applied Energy 100 (2012) 66–74

Contents lists available at SciVerse ScienceDirect

Applied Energy

journal homepage: www.elsevier.com/locate/apenergy

Syntheses of carbon porous materials with varied pore sizes and their performances as catalyst supports during methanol oxidation reaction

An-Ya Lo [a,b], Chin-Te Hung [a], Ningya Yu [c], Cheng-Tzu Kuo [d], Shang-Bin Liu [a,e,*]

[a] Institute of Atomic and Molecular Sciences, Academia Sinica, Taipei 10617, Taiwan
[b] Department of Materials Science and Engineering and Green Energy Development Center, Feng Chia University, Taichung 40724, Taiwan
[c] Department of Chemistry and Chemical Engineering, Hunan Normal University, Changsha 410081, China
[d] Department of Materials Science and Engineering, National Chiao Tung University, Hsingchu 30010, Taiwan
[e] Department of Chemistry, National Taiwan Normal University, Taipei 11677, Taiwan

HIGHLIGHTS

- CPMs with varied pore sizes (1–400 nm) were replicated from various porous silicas by CVI method.
- MOR activities of Pt/CPM electrocatalysts increase with increasing pore size of CPM support.
- Microporous CPMs are favorable supports for Pt in terms of catalytic performance and CO-tolerance.

ARTICLE INFO

Article history:
Received 3 April 2012
Received in revised form 26 April 2012
Accepted 6 May 2012
Available online 12 July 2012

Keywords:
Carbon porous materials
DMFC
Electrocatalyst
Methanol oxidation reaction
CO poisoning

ABSTRACT

Carbon porous materials (CPMs) with extended ranges of pore size and morphology were replicated using various porous silicas, such as zeolites, mesoporous silicas, and photonic crystals, as templates by means of chemical vapor infiltration (CVI) method. The micro-, meso-, and macro-porous carbons so fabricated were adopted as supports for the metal (Pt) catalyst for direct methanol fuel cells (DMFCs), and the supported Pt/CPM electrocatalysts were characterized by a variety of different spectroscopic/analytical techniques, *viz.* transmission electron microscopy (TEM), Raman, X-ray photoelectron spectroscopy (XPS), gas physisorption/chemisorption analyses, and cyclic voltammetry (CV). That these Pt/CPMs were found to exhibit superior electrocatalytic activities compared to the commercial Pt/XC-72 with a comparable Pt loading during methanol oxidation reaction (MOR) is attributed to the presence of Pt nanoparticles (NPs; typically 1–3 nm in size) that are highly dispersed in the CPMs, facilitating an improved tolerance for CO poisoning. While the MOR activity observed for various Pt/CPMs tend to increase with increasing pore size of the carbon supports, Pt catalyst supported on carbon substrates possessing microporosities was found to have superior stability in terms of tolerance for CO poisoning than those with greater pore size or having meso- and macroporosities.

© 2012 Elsevier Ltd. All rights reserved.

1. Introduction

In view of the increasing demands in environmental protection issues, proton exchange membrane fuel cell (PEMFC) and direct methanol fuel cells (DMFCs), which use hydrogen and methanol as the fuel, respectively, have emerging as promising renewable power devices [1–3]. Since the fabrication of electrocatalyst materials and membrane electrode assembly (MEA) are known to dictate the efficiency, stability, and cost of a fuel cell stack and that the electrocatalysts commonly used nowadays are mostly noble metal (Pt or Pt-based) alloys supported on carbon substrates [1,4–8]. As such, characteristics of the carbon support as well as that of the metal catalyst are critical to the overall electrocatalytic performance of the fuel cell electrodes [9,10]. Therefore, in addition to the metal catalysts, R&D of carbon materials, such as carbon porous materials (CPMs) [10–13], carbon nanotubes (CNTs) [6], and activated carbons [14], that possess high surface areas, electrical conductivities, and electrochemical stabilities have drawn considerable attentions.

Regarding to DMFC application and operation, catalytic activity during methanol oxidation reaction (MOR) and resistance to CO poisoning are the key issues engaged in R&D of Pt-based electrocatalysts at anode [11,15,16]. It is anticipated that supported electrocatalyst with a well-dispersed novel metal catalyst should has a better catalytic activity. Whereas to prevail over the CO poisoning problem, utilization of bifunctional metal catalysts such as Pt–Ru

* Corresponding author at: Institute of Atomic and Molecular Sciences, Academia Sinica, Taipei 10617, Taiwan. Fax: +886 2 23620200.
E-mail address: sbliu@sinica.edu.tw (S.-B. Liu).

0306-2619/$ - see front matter © 2012 Elsevier Ltd. All rights reserved.
http://dx.doi.org/10.1016/j.apenergy.2012.05.043

alloy supported on carbons have becoming the benchmark applications, particularly for DMFC at anode [11–13,17–18]. However, supported Pt–Ru catalysts are also drawback by their cost ineffectiveness, as a result, alternative CO tolerance bifunctional alloy catalysts, such as Pt–Fe, Pt–Co, Pt–Ni, and Pt–Mo, have been extensively studied [19,20]. Recently, it has been shown that by embedding the monofunctional Pt catalyst in CPMs with well-defined mesostructures, the supported Pt/CPM catalyst exhibits outstanding CO tolerance even without the incorporation of a secondary metal [11], while a detailed mechanism involved in the above finding is yet to be further explored, related research represent advanced development of DMFC electrocatalyst at anode.

As for the development of CPMs over the past few decades, the investigations were mostly focused on carbon mesoporous materials (CMMs) with pore size ranging from 2 to 50 nm, while overlooking the potential applications of microporous (pore size < 2 nm) and macroporous (pore size > 50 nm) carbons. To explore the effect of pore size of the CPMs on the electrocatalytic performance of the supported Pt/CPM catalyst for DMFC at anode, we have developed a template-assisted chemical vapor infiltration (CVI) process to facilitate easy fabrication of CPMs with unprecedented textural properties [21]. Accordingly, a series of CPMs with varied pore sizes ranging from micro-, meso-, to macro-porous carbons, namely the ZRC, CMT-1, CMT-2, HCC, and PCC materials (*vide infra*) were replicated by using zeolite Y, MCM-48, SBA-15, defective MCM-48, and photonic crystal as templates, respectively. These unique CPMs were adopted as supports to prepare various Pt/CPM anodic electrocatalysts for DMFC. The physicochemical properties as well as the electrocatalytic performances of the resultant Pt/CPMs during MOR were evaluated and compared with a commercial Pt/XC-72 catalyst (Johnson–Matthey; 10 wt.% Pt on Vulcan XC-72 activated carbon).

2. Experimental section

2.1. Preparation of porous silica templates

Microporous Faujasite (*Y*)-type zeolite (Si/Al = 2.49) was obtained from Strem Chemicals, Inc. Highly stable MCM-48 mesoporous silica material was synthesized following the procedures reported earlier [22]. In brief, surfactant mixture solution was first prepared by dissolving both CTABr (7.6532 g; Acros) and Brij-30 (1.45 g; Aldrich) simultaneously in distilled water (60 mL). Then, a sodium hydroxide solution (2.5 g in 5 mL water) was added to the aforementioned mixture solution under stirring condition (for 0.5 h) followed by adding the silica solution. The resultant mixture was shaken vigorously for 0.5 h, then, gel-like substrate was kept at 373 K for crystallization for 2 days. Subsequently, the pH of the substrate was adjusted to 10 and kept at 373 K for additional 2 days. Finally, the resulting product was filtered and washed, dried, and then calcined in air at 823 K for 6 h.

The SBA-15 mesoporous silica was also prepared following a known recipe [23] Typically, tetraethyl orthosilicate (TEOS, Aldrich), which was used as the silica source, was added to an aqueous solution containing HCl and triblock copolymer surfactant (P_{123}; Acros) at 313 K, with a starting weight ratio of: 2.3 g TEOS: 1.0 g P_{123}: 8.0 g HCl: 30.0 g H_2O. The mixture was stirred for about 2 h before it was aged at 373 K for 2 days. The final product was then filtered, washed, dried, and finally calcined in air at 833 K for 6 h to remove the surfactant template.

Photonic crystal (PC) macroporous silica was synthesized following the procedure reported by Holland et al. [24]. First, 1700 mL of DI water was heated to 343 K and then stirred with styrene (200 mL, Aldrich) under nitrogen atmosphere. Then, potassium persulfate solution (100 mL, 0.025 M, 343 K) was added into the above styrene solution and kept under stirring condition for 28 h to allow for polymerization. Finally, the poly-styrene latex spheres were gathered by filtering and drying in air, followed by a silica replication process by which millimeter-thick layers of latex spheres were deposited on a filter paper in a Buchner funnel under vacuum while soaked with ethanol. Then, TEOS was added drop-wise to cover the latex spheres completely during filtration. After drying the composite product in a vacuum evaporator, the latex spheres were collected and subjected to calcination treatment in air at 848 K for 7 h to obtain the photonic crystals with an averaged pore diameter of ca. 400 nm.

2.2. Preparation of carbon porous materials

Carbon mesoporous materials (CPMs) synthesized by replication method using various porous silicas templates were conducted by a similar CVI procedure summarized below: first, the templating substrate was placed into a quartz reactor, followed by heating the reactor to the target temperature (typically 1073 or 1093 K) under vacuum. Then, a desirable amount of acetylene, which served as the carbon source, was introduced into the reactor in form of mixture gas together with H_2 and/or Ar. Then, the CPMs products may be respectively collected by filtering and drying after removing the silica template by etching with 1 M HF solution of 50% ethonal–50% H_2O. Detailed preparation conditions and average pore size observed for various CPMs are depicted in Table 1.

2.3. Preparation of Pt/CPM electrocatalysts

To explore their applications as catalyst supports in DMFC at anode, a hydrogen reduction process was adopted to disperse noble metal (Pt) catalyst on various CPMs. Typically, this is done by first suspending ca. 0.2 g of the desirable CPM substrate in H_2PtCl_6 aqueous solution (10 mL H_2PtCl_6, 0.04 M) at room temperature (295 K), followed by drying the substrate in a vacuum evaporator, then, a reduction treatment at 523 K under H_2 environment for 0.5 h. Following the sample names designated for various CPMs, the resultant electrocatalysts are denoted as Pt/ZRC, Pt/CMT-1, Pt/CMT-2, Pt/HCC, and Pt/PCC, respectively.

2.4. Characterization methods

The structural properties of various samples were examined by TEM (JEOL, JEM-2100; at 200 keV) and XRD (PANalytical, X'Pert PRO; using Cu Kα radiation; λ = 0.1541 nm). Thermogravimetric analyses (TGA; Netzsch TG-209) of various samples were performed under dried air atmosphere, and their BET surface areas

Table 1
Synthesis conditions and pore diameters of various CPMs prepared by template-assisted CVI process.

Sample[a]	Δ*t* (min)[b]	Template[c]	Gas flow ratio ($C_2H_2/H_2/Ar$)[d]	T_S (K)[e]	*D* (nm)[f]
ZRC	40	Zeolite Y	50/50/50	1073	<1.3
CMT-1	40	MCM-48	50/50/50	1073	~2
CMT-2	60	SBA-15	50/50/0	1073	~3
HCC	40	Defected MCM-48	50/50/0	1093	20–150
PCC	120	Photonic crystal	50/50/0	1073	~400

[a] Prepared in the absence of a catalyst and without gas preheating; pressure = 3 kPa.
[b] Duration of processing time.
[c] Porous silica template used for producing CPMs.
[d] In unit of sccm:sccm:sccm.
[e] Substrate temperature during CVI process.
[f] Pore diameter of porous carbon.

and pore size distributions (PSDs) were evaluated by nitrogen adsorption/desorption measurements (using a Quantachrome Autosorb-1 analyzer) conducted at 77 K after each sample was degassed at 473 K under vacuum for at least 12 h.

The electrochemical properties of various supported Pt/CPMs substrates (as anodic electrode materials for DMFC) were evaluated by cyclic voltammetry (CV) measurements conducted on a galvanostat/potentiostat (Autolab, PGSTAT30). The electrocatalytic activity of various Pt/CPM samples with a typical Pt loading of ca. 10 wt.% were evaluated using a glassy carbon as the working electrode, Pt wire as the counter electrode, and Ag/KCl (3 M) as a reference electrode at a scanning rate of 10 mV/s. The glossy carbon thin-film electrode was prepared by the following steps: first, ca. 10 mg of PtRu-loaded carbon sample was added into 5 mL of deionized water, followed by an ultrasonic treatment for 0.5 h. Next, ca. 20 μL of the resultant suspension mixture was withdrawn and injected onto the glassy carbon electrode (ca. 5 mm in diameter), followed by drying in air at 333 K for 1 h. Finally, 20 μL of 1% Nafion (DuPont) solution was added as a binder under N_2 environment. Electrooxidation of MeOH was carried out with an electrolyte of 0.5 M H_2SO_4 and 1 M MeOH between −0.2 and 1.0 V at room temperature. Prior to each CV measurement, the electrolytic solution was purged with high-purity N_2 (99.9%) for at least 0.5 h to remove the dissolved oxygen; subsequently, the experiment was conducted under purging N_2 condition. For comparison, similar measurements were also performed on a commercial Pt/XC-72 catalyst (Johnson–Matthey; 10 wt.% Pt on Vulcan XC-72).

The dispersions of Pt on various Pt/CPM samples were measured by hydrogen chemisorption. For each run, ca. 0.02 g of Pt/CPM sample was pretreated by outgassing at 623 K for 1 h, then, the first H_2 adsorption isotherm was measured after the sample was cooled to 305 K, followed by outgassing the substrate for 1 h to obtain a second H_2 adsorption isotherm under the same condition. On the other hand, CO tolerance tests were done by competitive adsorption with H_2 on an automated chemisorption apparatus (Micromeritics, AutoChem II 2920). First, ca. 500 ppm of CO was pre-adsorbed onto the sample at 328 K for 0.5 h, then H_2 (10%) was pluse-injected using Ar as the carrier gas till a saturated coverage of H_2 was achieved.

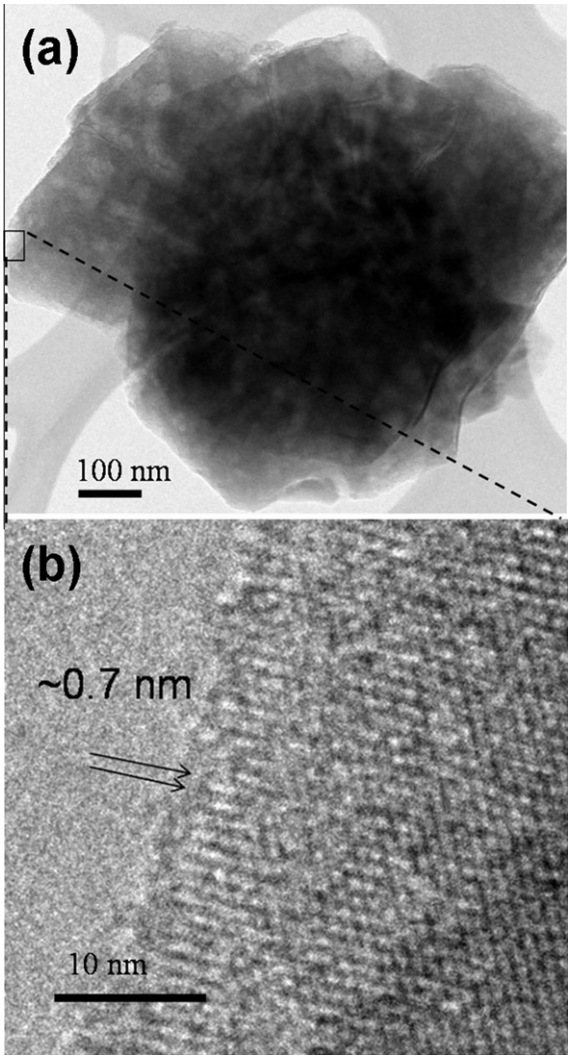

Fig. 1. (a) TEM and (b) HRTEM image of the zeolite *Y* template.

3. Results and discussion

3.1. Structural properties of CPMs

Figs. 1 and 2 display the TEM images of zeolite *Y* and its corresponding carbon replica, namely the zeolite replicated carbon (ZRC). The high resolution image of Fig. 1b clearly indicates the ordered framework structure of zeolite *Y* with a pore aperture of ca. 0.7 nm, which is typical for 12-membered ring zeolites [25]. That the ZRC material (Fig. 2a) possesses a similar morphology with zeolite *Y* (Fig. 1a) suggests that the CVI process so utilized readily prevail even for replication of microporous systems. As a consequence, ZRC is found to possess tubular carbon with an average diameter as small as 0.7 nm, as shown in Fig. 2b. Such template-assisted CVI process therefore represents a facile and speedy synthesis route for CPMs. As can be seen from Table 1, the time required for fabrication of CMPs is typically within two hours. It is noteworthy that, unlike its zeolitic template, which possesses a well-ordered structure (Fig. 1b), the structure of ZRC appears to lack long-range ordering (Fig. 2b), as also revealed by the XRD results in Fig. 3.

The N_2 adsorption/desorption curves obtained from the ZRC material in Fig. 4a showed a typical type-I isotherm, in which the abrupt rise of the isotherm at low relative pressure (i.e., Henry's Law region) reveals the existence of micropores in the sample; in line with the TEM (Fig. 2b) and PSD (Fig. 5a) results. A rough estimation of the latter by the BJH method (which may be unjustifiable for micropore analysis) led to an average pore size of ca. 1.3 nm for the tubular ZRC, which coincides with the size of the sodalite building unit of Faujasite-type zeolites (ca. 1.2 nm) [25].

Previously, we reported the syntheses of CMT-1 [5] and HCC [21] by the similar CVI process. While both CMT-1 and HCC may both be replicated using mesoporous MCM-48 silica as the template, they were fabricated at different carbonization temperatures, namely 1073 and 1093 K, respectively (Table 1). Similar to that reported for mesoporous CMK-1 carbon [26–29], the N_2 adsorption/desorption isotherms obtained from CMT-1 shown in Fig. 4b exhibited the typical type-IV isotherm with a broad hysteresis loop, which is a typical signature for capillary condensation in mesoporous channels [30–32]. As can be seen from the PSD profile in Fig. 5b, the CMT-1 possesses pore sizes around 2–3 nm. However, the mesostructure of the MCM-48 silica tends to partially collapse upon further increasing the carbonization temperature to 1093 K, leading to mesoporous carbon (denoted as HCC) with a defective structure that exhibits a broad PSD centered at ca. 20 nm (Fig. 6a). Such a broad distribution of pore sizes was derived from the N_2 adsorption/desorption data in Fig. 4d, which showed a typical type-IV isotherm with type-H3 hysteresis loop. As such, the HCC material is most likely consists of plate-like aggregates of particles giving rise to slit-shaped pores [5,33]. Similar to CMT-1, the

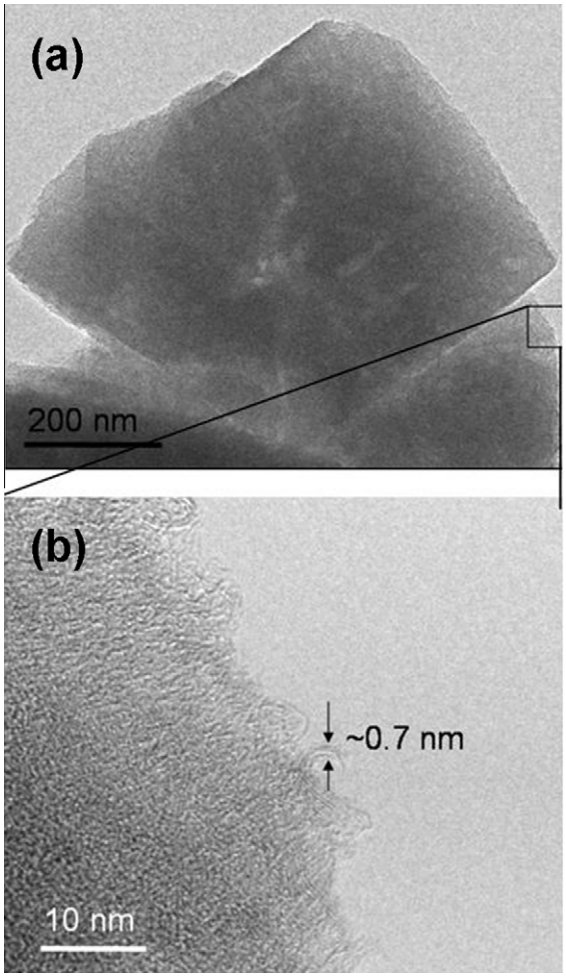

Fig. 2. (a) TEM and (b) HRTEM image of the synthesized ZRC material.

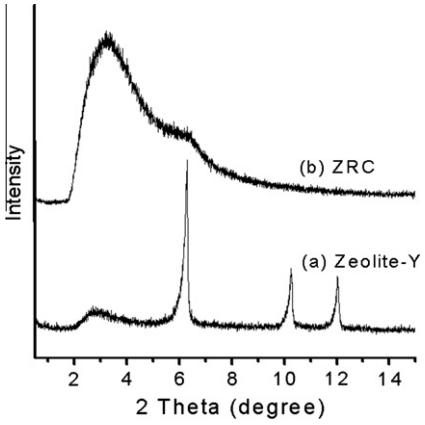

Fig. 3. XRD patterns of (a) zeolite *Y* and (b) ZRC materials.

CMT-2 carbon replicated from mesoporous SBA-15 silica also exhibited a type-IV isotherm (Fig. 4c) and a uniform pore size of ca. 3 nm (Fig. 5c). The TEM image (Fig. 7b) and the XRD profile (Fig. 8b) further indicate the existence of long-range structure ordering with 2-D hexagonal symmetry similar to that of tubular CMK-5 mesoporous carbon [34].

To fabricate macroporous carbon, photonic crystal (PC) with pore diameter of ca. 400 nm (Fig. 9a) [24] was utilized as the silica template. The resultant carbon so synthesized, denoted as PCC, also

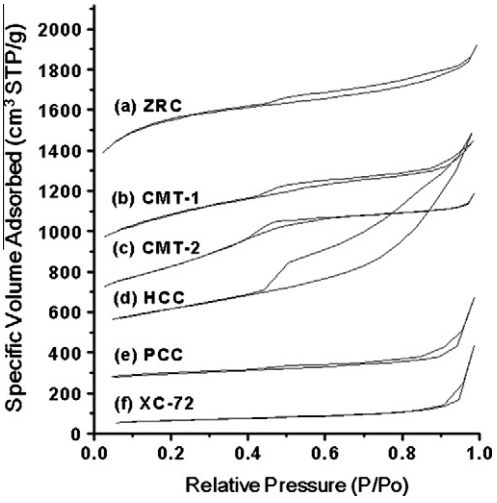

Fig. 4. N_2 adsorption/desorption isotherms (77 K) of (a) ZRC, (b) CMT-1, (c) CMT-2, (d) HCC, (e) PCC, and (f) XC-72. The vertical scales for (a)–(e) were shifted by 1000, 800, 600, 400, and 200 cm^3 STP/g, respectively.

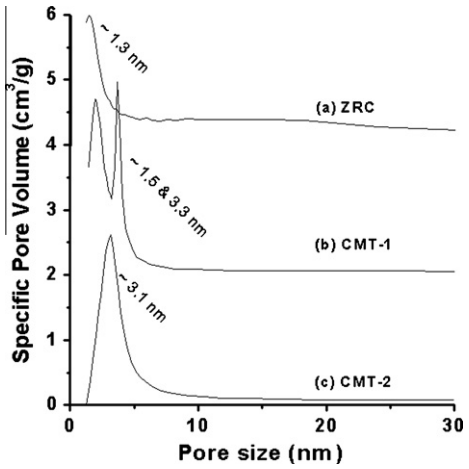

Fig. 5. BJH pore size distributions of (a) ZRC, (b) CMT-1, and (c) CMT-2. The vertical scale for (a) and (b) were shifted by 4 and 2 cm^3/g, respectively.

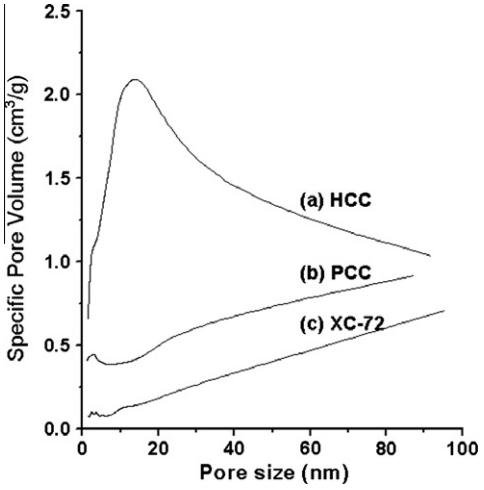

Fig. 6. BJH pore size distributions of (a) HCC, (b) PCC, and (c) XC-72. The vertical scale for (a) and (b) were shifted by 0.5 and 0.25 cm^3/g, respectively.

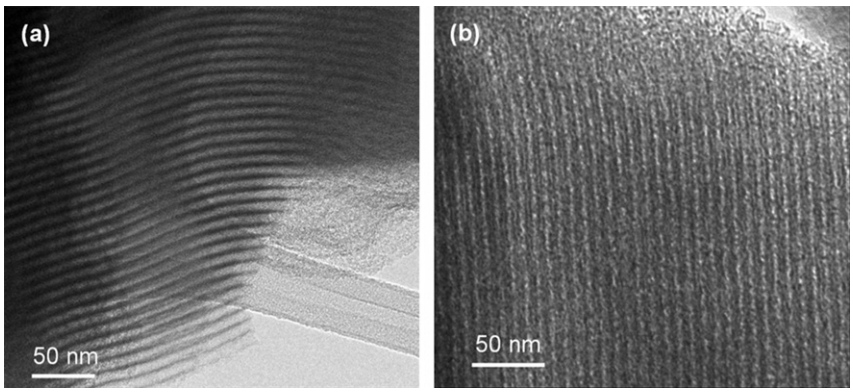

Fig. 7. TEM images of (a) SBA-15 and (b) CMT-2 materials.

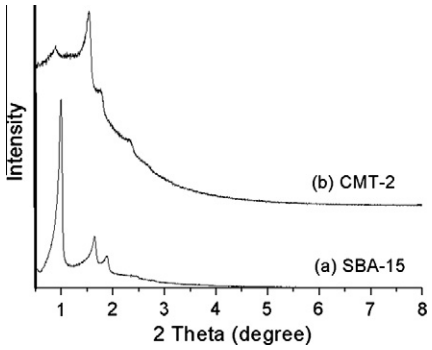

Fig. 8. XRD patterns of (a) SBA-15 and (b) CMT-2 materials.

reveal a similar pore diameter of ca. 400 nm (Fig. 9b). Resembling the XC-72 activated carbon (Fig. 4f), the N_2 adsorption/desorption isotherms obtained from the PCC sample (Fig. 4e) also exhibit a type-III isotherm, typical for macroporous materials [33]. Nevertheless, unlike the HCC material, the PSDs of both PCC (Fig. 6b) and XC-72 (Fig. 6c) failed to represent the truth surface condition shown in Fig. 9. This is ascribed due to the extensive pore size and inter-particle surfaces present in these porous carbon samples. For comparison, the specific surface area and pore distribution for various CPMs and XC-72 are depicted in Table 2. Since its BET surface area may not be readily derived from the N_2 isotherm data for macropores, total surface areas of PCC and XC-72 were depicted in Table 2. In this context, the external surface area should be analogous to the internal surface area for the PCC material.

Table 2
Comparison of specific surface areas for various CPM samples.

Sample	Specific surface area (m^2/g)[a]		
	Micropores	Mesopores	Macropores
ZRC	1235	647[b]	N/A
CMT-1	←1229[c]→		N/A
CMT-2	N/A	1194	N/A
HCC	N/A	←783[d]→	
PCC	N/A	N/A	337
XC-72	N/A	N/A	218

[a] N/A: surface area in these ranged are either negligible or unaccountable by the BJH method.
[b] Value estimated by subtracting the microporous surface area (determined by *t*-plot analysis) from the total BET surface area.
[c] CMT-1 possesses two types of pore systems, which span over the micro- and mesoporous ranges.
[d] Since its BET surface area may not be derived in this pore range, total surface area of the substrate was adopted.

3.2. Effect of pore size of the carbon support on electrocatalytic performance of Pt/CPM

Upon incorporating the Pt catalyst (typically ca. 9–13 wt.%) onto various CPM supports, each Pt/CPM sample was subjected to a reduction treatments under H_2 at 523 K. The physicochemical properties of various supported Pt/CPM catalysts are depicted in Table 3 along with that of a commercial Pt/XC-72 catalyst. On

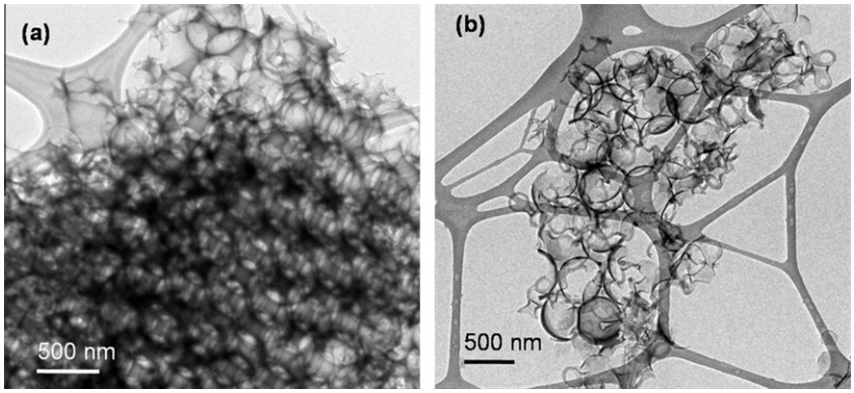

Fig. 9. TEM images of (a) PC and (b) PCC materials.

Table 3
Assorted physicochemical properties of various Pt/CPMs and Pt/XC-72 electrocatalysts.

Catalyst	*Pt* (wt.%)[a]	*C* (S/cm)[b]	I_G/I_D[c]	I_f (mA)	I_r (mA)	I_f/I_r[d]	Δ_{Pt} (%)[e]	D_p (nm)[f]	S_M (m^2/g Pt)[g]	*CO-t* (%)[h]
Pt/ZRC	12.5	1.61	0.85	122	25	4.88	45.4	2.49	112.1	48.83
Pt/CMT-1	12.8	1.14	0.68	136	60	2.26	22.4	5.05	55.4	27.93
Pt/CMT-2	11.6	1.10	0.77	140	97	1.44	19.8	5.71	48.9	18.14
Pt/HCC	9.3	2.07	0.74	282	194	1.45	20.5	5.51	50.7	10.60
Pt/PCC	9.5	2.38	0.73	655	628	1.04	56.8	1.99	140.4	7.78
Pt/XC72	12.5	1.79	0.70	353	349	1.01	32.6	3.47	80.6	1.74

[a] Pt loading determined by TGA analysis.
[b] Electrical conductivity.
[c] Relative peak intensities obtained from the G- and D-bands of the Raman spectrum.
[d] Ratio of maximum current densities obtained from the forward (I_f) and reverse (I_r) scans of the CV curves.
[e] Pt dispersion measured by H_2 chemisorption (at 305 K).
[f] Pt particle size derived from H_2 chemisorption results.
[g] Metallic surface area of the Pt nanoparticles derived from H_2 chemisorption.
[h] CO-tolerance estimated by competitive adsorption of H_2 after pre-adsorbing ca. 500 ppm of CO.

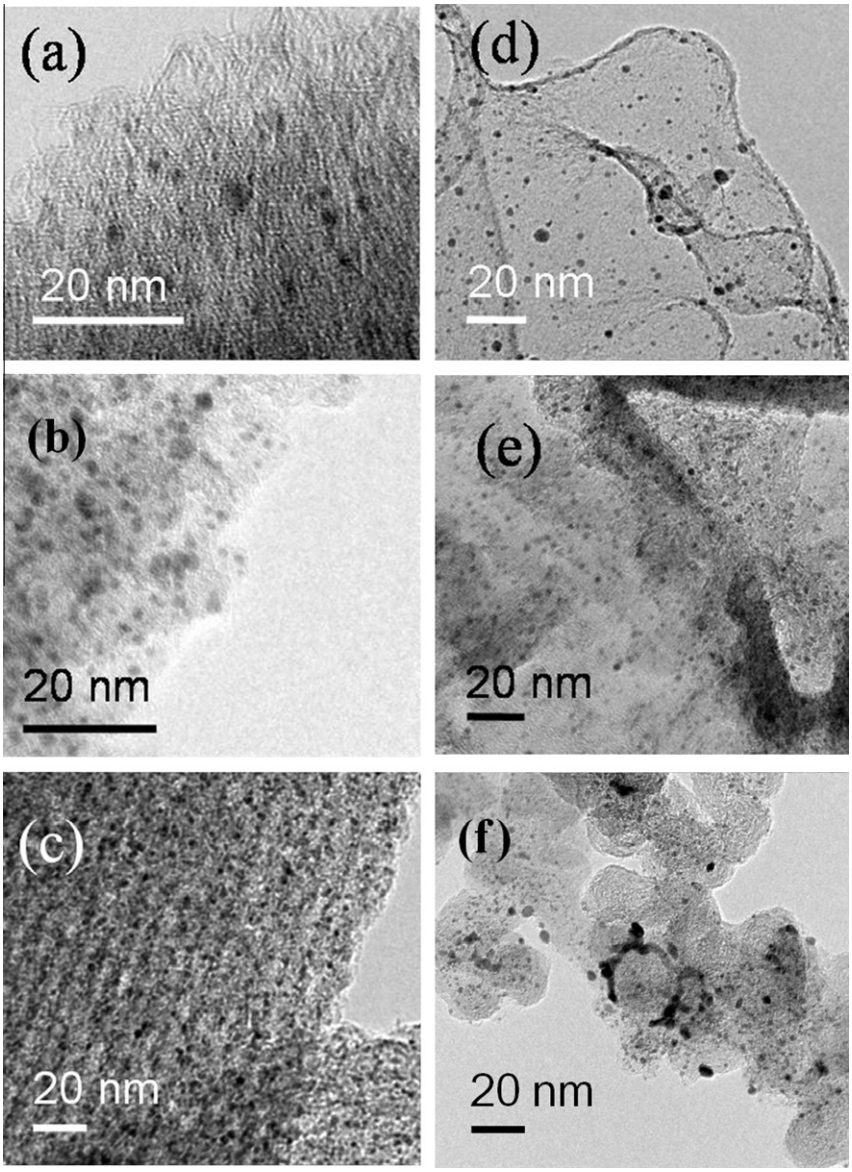

Fig. 10. TEM images of (a) Pt/ZRC, (b) Pt/CMT-1, (c) Pt/CMT-2, (d) Pt/HCC, (e) Pt/PCC, and (f) Pt/XC-72 electrocatalysts.

the basis of the similarities in electrical conductivity (*C*) and I_G/I_D (i.e., the peak intensity ratio obtained from the G- and D-bands of the Raman spectrum, which corresponds to the relative concentration of sp^2 and sp^3 structures of the carbon substrate)

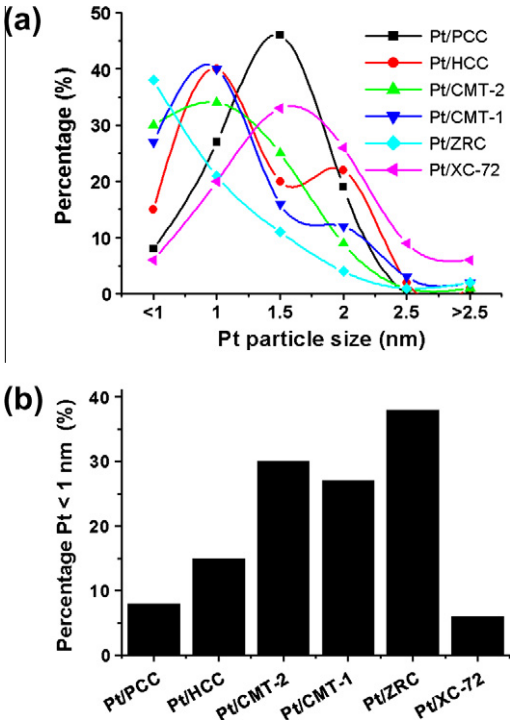

Fig. 11. Pt particle size distributions of various Pt/CPM electrocatalysts, (a) the overall profile and (b) histogram for particle size < 1 nm only.

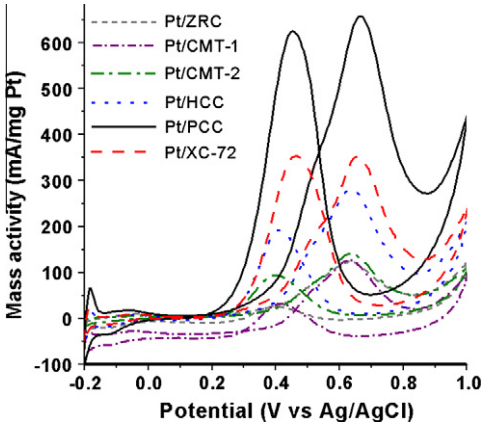

Fig. 12. Room temperature cyclic voltammograms of various Pt/CPMs and Pt/XC-72 electrocatalysts in solution of 0.5 M H_2SO_4 and 1 M MeOH.

values, it is indicative that all supported electrocatalysts have roughly the same degree of graphitization and hence similar electronic properties.

The TEM images of various Pt/CPM supported catalysts are depicted in Fig. 10. Among them, the Pt/ZRC and Pt/PCC samples appear to have the highest Pt dispersion (Δ_{Pt}; see Table 3). A closer examination on the Pt particle size distribution (Fig. 11a) revealed that, unlike Pt/PCC in which a rather uniform Pt particle size distribution centered at ca. 1.5 nm, majority of the Pt nanoparticles in Pt/ZRC were found less than 1 nm. This may be attributed to the fact that the ZRC support possesses only microporosities. As such, it is hypothesized that the porosity of the carbon support may play an important role while incorporating the Pt metal catalyst. By comparison, the percentage of the small (size < 1 nm; Fig. 11b) Pt nanoparticle presented in various carbon supports appear to follow the trend: Pt/ZRC (38%) > Pt/CMT-2 (30%) ~ Pt/CMT-1 (27%) > Pt/HCC (15%) > Pt/PCC (8%) ~ Pt/XC-72 (6%). Consequently, the former

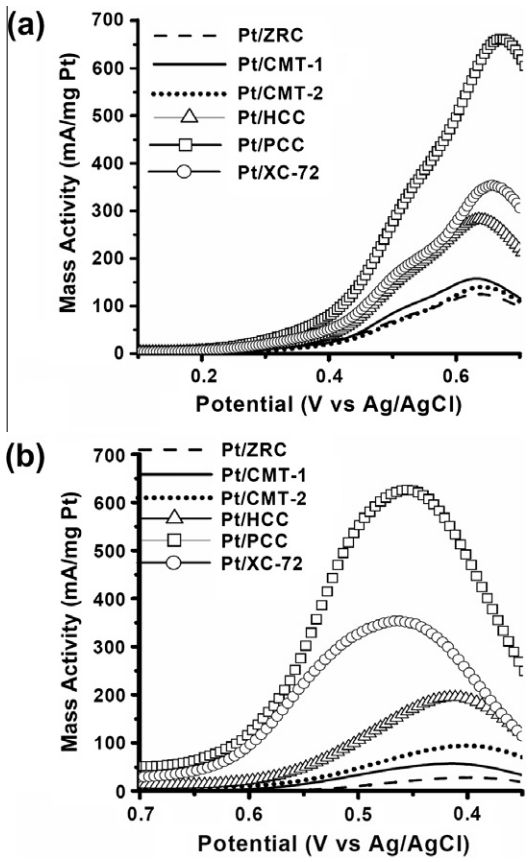

Fig. 13. (a) Forward and (b) reverse CV scans of various Pt/CPMs and Pt/XC-72 electrocatalysts.

shows a high metallic surface area and superior electrocatalytic performances (see Table 3) in terms of I_f/I_r ratio and resistance to CO poisoning, i.e. *CO-t* value (*vide infra*).

Fig. 12 shows the cyclic voltammograms of various Pt/CPMs and Pt/XC-72 electrocatalysts under in solution of 0.5 M H_2SO_4 and 1 M MeOH. Since the mass activity of the anodic peak occurred at ca. 0.6 V during the forward scan (I_f) is associated with the catalytic activity during methanol oxidation reaction (MOR), whereas that of the reversed peak (I_r; at ca. 0.4–0.5 V) is mainly related to the extent of deactivation due to deposition of carbonaceous residues on the surfaces of the catalyst [12,35]. For purpose of comparison, the CV curves observed from various catalyst samples in selected operating potential region of 0.1–0.65 V and 0.7–0.45 V are displayed for forward (Fig. 13a) and reverse (Fig. 13b) scans, respectively. Assorted physicochemical properties, such as electrical conductivity (C), I_G/I_D ratio, current densities (I_f and I_r), and dispersion (Δ_{Pt}), particle size (D_p), and metallic surface areas (S_M) of the Pt nanoparticles, are depicted in Table 3 together with the index *CO-t* representing the stability of the electrocatalyst in terms of tolerance for CO poisoning.

By careful examination of the experimental results listed in Table 3, it is found that, while the Pt/ZRC exhibited a superior electrocatalytic performance compared to the other Pt/CPMs anodic catalysts due to the more abundant Pt nanoparticles with size < 1 nm (*vide supra*), notably lower forward (I_f) and reverse (I_r) peak current densities were observed even though a somewhat higher I_G/I_D ratio was evident. In this context, the degree of graphitization and the electrical conductivity (C) of the CPM appear irrelevant to the values of I_f and I_r, rather, the latter tends to increase with increasing pore size of the carbon support (*cf.* Table 1). This may be ascribed due to the possibility that some of the Pt nanoparticles in CPMs may not be accessed by the methanol reactant

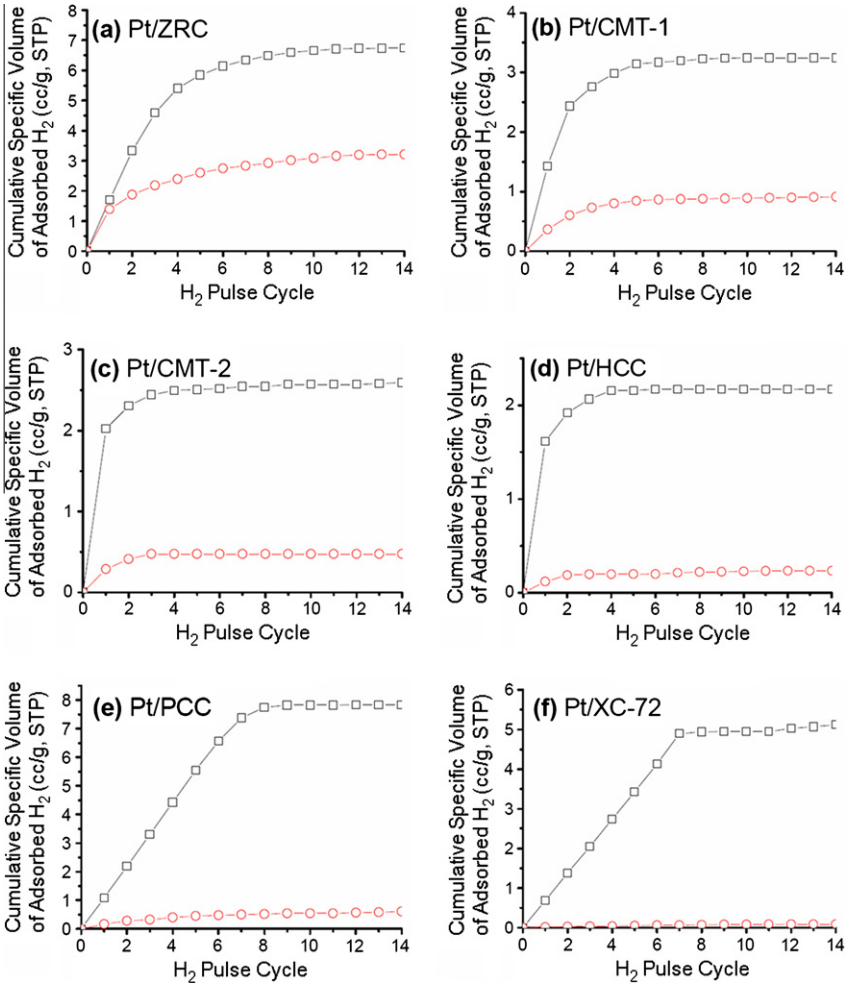

Fig. 14. Pulsed H_2 chemisorption profiles of (a) Pt/ZRC, (b) Pt/CMT-1, (c) Pt/CMT-2, (d) Pt/HCC, (e) Pt/PCC, and (f) Pt/XC-72 electrocatalysts without (square symbol) and with (circular symbol) pre-adsorption treatment by CO (500 ppm). The interval between H_2 pulse cycles was 5 min.

during the CV measurement. In other words, diffusion of methanol may be partially hindered in the pore channels of the CPMs. Nonetheless, notably higher I_f and I_r values were observed for CPMs supports possessing macroporosities, e.g., Pt/HCC, Pt/PCC, and Pt/XC-72 (Tables 2 and 3). Thus, it is indicative that the internal surface areas within the CPM supports containing micro- and/or mesoporosities have negligible effect on the overall electrocatalytic performance of the Pt/CPM electrocatalyst. Indeed, the Pt/ZRC, Pt/CMT-1 and Pt/CMT-2 showed relatively lower I_f and I_r values compared to Pt/HCC, Pt/PCC, and Pt/XC-72, whose surface areas arise predominantly from the external surfaces of the carbon supports. In short, it may be concluded that the MOR activity observed for various Pt/CPMs examined herein tend to increase with increasing pore size of the carbon supports. These observations therefore disclose a crucial parameter to improve the electrocatalytic performance of the Pt/CPM catalysts for application in DMFC at anode.

In terms of stability of the Pt/CPM electrocatalyst over the tolerance for CO poisoning (i.e., *CO-t* value), the ratio of maximum forward vs. reserve current densities, namely the I_f/I_r ratio, may be served as an index for assessment [15,36,37]. It is intriguing that the I_f/I_r value observed for various Pt/CPMs electrocatalysts tends to obey the trend (*cf.* Table 3): Pt/ZRC(4.88) >> Pt/CMT-1(2.26) >> Pt/CMT-2(1.44) ~ Pt/HCC(1.45) > Pt/PCC(1.04) ~ Pt/XC-72(1.01). In other words, the observed I_f/I_r value appears to decrease notably with increasing pore size of the porous carbon support. Moreover, it is indicative that Pt catalyst supported on carbon substrates possessing microporosities (e.g., ZRC and CMT-1; see Table 2) show much higher electrocatalytic stabilities than those having meso- and macroporosities. Note that the aforementioned trend also coincides with the amount of small Pt nanoparticles (<1 nm) dispersed within the porous carbon supports (*vide supra*).

To further justify the above findings, additional pulsed H_2 chemisorption measurements were conducted with and without the presence of pre-adsorbed CO (ca. 500 ppm). The results obtained from such competitive chemisorption of CO with H_2 for various Pt/CPMs and Pt/XC-72 electrocatalysts as shown in Fig. 14. Accordingly, the corresponding Δ_{Pt}, D_p, and S_M of the Pt nanoparticles, as well as the *CO-t* values are depicted in Table 3. For examples, a S_M value of ca. 112 m^2/g Pt was obtained for the Pt/ZRC sample, among them, ca. 47% of the metal surfaces remain active even after the catalyst was intentionally poisoned by pre-adsorbing 500 ppm of CO. Whereas in the case of Pt/XC-72, nearly all Pt surfaces were inactivated by the pre-adsorbed CO. Consequently, a similar trend mentioned earlier for the I_f/I_r values observed for various Pt/CPMs and Pt/XC-72 electrocatalysts may also be inferred for the observed *CO-t* (Table 3). In other words, Pt catalyst supported on carbon substrates possessing microporosities appears to have superior stability in terms of tolerance for CO poisoning over those with greater pore size or having meso- and macroporosities. Thus, it is the pore size of the carbon supports and the amount of accessible small (<1 nm) Pt nanoparticles that are crucial in dictating the electrocatalytic activity and the stability of anodic Pt/CPM catalysts for applications in DMFC during MOR. In this context, the overall dispersion (Δ_{Pt}), average particle size (D_p),

and total metallic surface areas (S_M) of the metal catalyst itself, play only relatively minor role, particularly in electrocatalytic performance (i.e., I_f/I_r ratio) and stability of the Pt/CPM electrocatalyst in terms of CO-tolerance.

4. Conclusions

Various carbon porous materials (CPMs), namely ZRC, CMT-1, CMT-2, HCC, and PCC, were successfully synthesized by template-assisted CVI process using porous silica templates with varied pore size from ca. 0.7 to 400 nm. It was found that carbon supports with smaller pore dimensions are more favorable for dispersing Pt nanoparticles with sub-nanometer sizes. However, microporosity presence in the CPM support may also hinder diffusion of reactant and product during MOR, which in turn diminishes the overall catalytic performance of the Pt/CPM catalyst. On the other hand, macroporous CPMs, which normally possess a large external surface area, exhibit superior catalytic performance during MOR. However, in terms of electrocatalytic stability of the anodic catalyst, Pt catalyst supported on CPM substrates possessing microporosities are found to exhibit superior tolerance for CO poisoning than those with greater pore size or having meso- and macroporosities. Thus, the pore size of the carbon supports and the amount of accessible small (<1 nm) Pt nanoparticles, rather than the overall dispersion (Δ_{Pt}), average particle size (D_p), or total metallic surface areas (S_M) of the Pt catalyst, play the crucial role in dictating the electrocatalytic activity as well as the stability of anodic Pt/CPM catalysts for applications in DMFC during MOR. These results also reveal an alternative and practical approach to overcome the critical CO poisoning problem during operation of DMFC without incorporating a secondary metal (such as Ru or transition metals) in the supported catalyst. Moreover, the results report herein also implies that Pt-based electrocatalyst supported on microporous carbons may have perspective applications in PEMFC and DMFC at anode.

Acknowledgements

The supports of this work by the National Science Council, Taiwan (NSC 98-2113-M-001-017-MY3 to SBL; and NSC 101-2218-E-035-005 to AL) are gratefully acknowledged. The authors thank Drs. Shou-Heng Liu and Zhibin Lei for helpful discussions.

References

[1] Wang Y, Chen KS, Mishler J, Cho SC, Adroher XC. A review of polymer electrolyte membrane fuel cells: technology, applications, and needs on fundamental research. Appl Energ 2011;88(4):981–1007.
[2] Achmad F, Kamarudin SK, Daud WRW, Majlan EH. Passive direct methanol fuel cells for portable electronic devices. Appl Energ 2011;88(5):1681–9.
[3] Tang Y, Yuan W, Pan M, Wan Z. Experimental investigation on the dynamic performance of a hybrid PEM fuel cell/battery system for lightweight electric vehicle application. Appl Energ 2011;88(1):68–76.
[4] Yuan W, Tang Y, Yang X, Wan Z. Porous metal materials for polymer electrolyte membrane fuel cells – A review. Appl Energ 2012;94(1):309–29.
[5] Lo AY, Liu SH, Huang SJ, Kuo CT, Liu SB. Hollowed carbon capsule based Pt-Fe/carbon electrodecatalysts prepared by chemical vapor infiltration method. Diam Relat Mater 2008;17(7–10):1541–4.
[6] Lo AY, Yu N, Huang SJ, Hung CT, Liu SH, Lei Z, et al. Fabrication of CNTs with controlled diameters and their applications as electrocatalyst supports for DMFC. Diam Relat Mater 2011;20(3):343–50.
[7] Zamel N, Li X, Shen J. Numerical estimation of the effective electrical conductivity in carbon paper diffusion media. Appl Energ 2012;93(1):39–44.
[8] Seo SH, Lee CS. A study on the overall efficiency of direct methanol fuel cell by methanol crossover current. Appl Energ 2010;87(8):2597–604.
[9] Qi J, Jiang L, Tang Q, Zhu S, Wang S, Yi B, et al. Synthesis of graphitic mesoporous carbons with different surface areas and their use in direct methanol fuel cells. Carbon 2012;50(8):2824–31.
[10] You DJ, Kwon K, Joo SH, Kim JH, Kim JM, Pak C, et al. Carbon-supported ultrahigh loading Pt nanoparticle catalyst by controlled overgrowth of Pt: Improvement of Pt utilization leads to enhanced direct methanol fuel cell performance. Int J Hydrogen Energ 2012;37(8):6880–5.
[11] Liu SH, Lu RF, Huang SJ, Lo AY, Chien SH, Liu SB. Controlled synthesis of highly dispersed platinum nanoparticles in ordered mesoporous carbons. Chem Commun 2006;32:3435–7.
[12] Liu SH, Yu WY, Chen CH, Lo AY, Hwang BJ, Chien SH, et al. Fabrication and characterization of well-dispersed and highly stable PtRu nanoparticles on carbon mesoporous material for applications in direct methanol fuel cell. Chem Mater 2008;20(4):1622–8.
[13] Maiyalagan T, Alaje TO, Scott K. Highly Stable Pt–Ru nanoparticles supported on three-dimensional cubic ordered mesoporous carbon (Pt–Ru/CMK-8) as promising electrocatalysts for methanol oxidation. J Phys Chem C 2011;116(3):2630–8.
[14] Park GG, Yang TH, Yoon YG, Lee WY, Kim CS. Pore size effect of the DMFC catalyst supported on porous materials. Int J Hydrogen Energ 2003;28(6):645–50.
[15] Zeng D, Pan M, Wang L, Tang Y. Fabrication and characteristics of cube-post microreactors for methanol steam reforming. Appl Energ 2012;91(1):208–13.
[16] Wijaya WY, Kawasaki S, Watanabe H, Okazaki K. Damköhler number as a descriptive parameter in methanol steam reforming and its integration with absorption heat pump system. Appl Energ 2012;94(1):141–7.
[17] Ren XM, Zelenay P, Thomas S, Davey J, Gottesfeld S. Recent advances in direct methanol fuel cells at Los Alamos National Laboratory. J Power Sources 2000;86(1–2):111–6.
[18] Lin ML, Lo MY, Mou CY. PtRu nanoparticles supported on mesoporous carbon thin film as highly active anode materials for direct methanol fuel cell. Catal Today 2011;160(1):109–15.
[19] Xu J, Hua K, Sun G, Wang C, Lv X, Wang Y. Electrooxidation of methanol on carbon nanotubes supported Pt–Fe alloy electrode. Electrochem Commun 2006;8(6):982–6.
[20] Zhao H, Dong J, Xing S, Li Y, Shen J, Xu J. Electrochemical oxidation of small organic molecules on hydrothermal synthesized Pt and PtCo/ordered mesoporous carbon. Int J Hydrogen Energ 2011;36(16):9551–61.
[21] Lo AY, Huang SJ, Chen WH, Peng YR, Kuo CT, Liu SB. Template-assisted synthesis of mesoporous tubular carbon nanostructure by chemical vapor infiltration method. Thin Solid Films 2006;498(1–2):193–7.
[22] Kim JM, Kim SK, Ryoo R. Synthesis of MCM-48 single crystals. Chem Commun 1998;2:259–60.
[23] Zhao D, Feng J, Huo Q, Melosh N, Fredrickson GH, Chmelka BF, et al. Triblock copolymer syntheses of mesoporous silica with periodic 50–300 angstrom pores. Science 1998;279(5350):548–52.
[24] Holland BT, Blanford CF, Do T, Stein A. Synthesis of highly ordered, three-dimensional, macroporous structures of amorphous or crystalline inorganic oxides, phosphates, and hybrid composites. Chem Mater 1999;11(3):795–805.
[25] Nagy JB, Bodart P, Hannus I, Kiricsi I. Synthesis, characterization and use of zeolite microporous materials. Szeged (Hungary): Deca Gen Ltd.; 1998.
[26] Ryoo R, Joo SH, Kim JM. Energetically favored formation of MCM-48 from cationic-neutral surfactant mixtures. J Phys Chem B 1999;103(35):7435–40.
[27] Joo SH, Jun S, Ryoo R. Synthesis of ordered mesoporous carbon molecular sieves CMK-1. Micropor Mesopor Mat 2001;44–45(1):153–8.
[28] Kaneda M, Tsubakiyama T, Carlsson A, Sakamoto Y, Ohsuna T, Terasaki O, et al. Structural study of mesoporous MCM-48 and carbon networks synthesized in the spaces of MCM-48 by electron crystallography. J Phys Chem B 2002;106(6):1256–60.
[29] Ohkubo T, Miyawaki J, Kaneko K, Ryoo R, Seaton NA. Adsorption properties of templated mesoporous carbon (CMK-1) for nitrogen and supercritical methane – Experiment and GCMC simulation. J Phys Chem B 2002;106(25):6523–8.
[30] Sing KSW, Everett DH, Haul RAW, Moscou L, Pierotti RA, Rouquerol J, et al. Reporting physisorption data for gas solid systems with special reference to the determination of surface-area and porosity. Pure Appl Chem 1985;57(4):603–19.
[31] Ravikovitch PI, Neimark AV. Density functional theory of adsorption in spherical cavities and pore size characterization of templated nanoporous silicas with cubic and three-dimensional hexagonal structures. Langmuir 2002;18(5):1550–60.
[32] Matos JR, Kruk M, Mercuri LP, Jaroniec M, Zhao L, Kamiyama T, et al. Ordered mesoporous silica with large cage-like pores: Structural identification and pore connectivity design by controlling the synthesis temperature and time. J Am Chem Soc 2003;125(3):821–9.
[33] Lowell S, Shields JE, Thomas MA, Thommes M. Characterization of porous solids and powders: surface area, pore size and density. Dordrecht: Kluwer Academic Publishers; 2004.
[34] Joo SH, Choi SJ, Oh I, Kwak J, Liu Z, Terasaki O, et al. Ordered nanoporous arrays of carbon supporting high dispersions of platinum nanoparticles. Nature 2001;412(6843):169–72.
[35] Lei Z, Zhao M, Dang L, An L, Lu M, Lo AY, et al. Structural evolution and electrocatalytic application of nitrogen-doped carbon shells synthesized by pyrolysis of near-monodisperse polyaniline nanospheres. J Mater Chem 2009;19(33):5985–95.
[36] Choudhary VR, Mondal KC. CO_2 reforming of methane combined with steam reforming or partial oxidation of methane to syngas over $NdCoO_3$ perovskite-type mixed metal-oxide catalyst. Appl Energ 2006;83(9):1024–32.
[37] Kwak BS, Lee JS, Lee JS, Choi BH, Ji MJ, Kang M. Hydrogen-rich gas production from ethanol steam reforming over Ni/Ga/Mg/Zeolite *Y* catalysts at mild temperature. Appl Energ 2011;88(12):4366–75.